Electronic Supplementary Material (ESI) for Soft Matter.

Supplementary Information

Measuring Colloid-Surface Interaction Forces in Parallel Using Fluorescence Centrifuge Force Microscopy

Thomas B. LeFevre[1,2], Dimitri A. Bikos[1,2], Connie B. Chang[1,2], and James N. Wilking[1,2]*
[1]Department of Chemical and Biological Engineering,
[2]Center for Biofilm Engineering,
Montana State University, Bozeman, MT, USA

Table of Contents:

SI Notes:

SI Note 1: Measuring the swinging bucket angle as a function of centrifuge rotational velocity

A hole was drilled in the bottom of one of the swinging buckets. The brightfield LED was soldered upside down into the PCB so that it pointed down through the bucket hole instead of up towards the sample (**SI Fig. 2A**). A new F-CFM clamshell holder was printed to accommodate the LED pointing downwards. A piece of photosensitive cyanotype paper (stevespanglerscience.com) was taped to the wall of the centrifuge. The centrifuge was closed and allowed to run at a constant speed for 20 min, with the LED light creating a line in the photosensitive paper. The centrifuge was then opened, and the bucket held such that the LED pointed at the line it created. Then a digital angle finder was held against the bucket to determine its angle in that position (**SI Fig. 2B**). This process was repeated throughout the speed range of the centrifuge. The visibility of the line created by the LED on the photosensitive paper was improved slightly after developing in water (**SI Fig. 2C**).

SI Note 2: F-CFM Assembly

The F-CFM is assembled as follows. The camera (**SI Fig. 1a**) is prepared using pliers to unscrew the commercial lens from the camera. The camera is attached to the microscope via a hand-fabricated M12 externally threaded aluminum tube (**SI Fig. 1b**) which is connected to a Thorlabs M12-SM1 adapter (**SI Fig. 1c**) screwed into a 1-in long Thorlabs SM1 lens tube (**SI Fig. 1d**). Retaining rings (**SI Fig. 1e**) hold a focusing lens (**SI Fig. 1f**) in this same tube. The fluorescence cube (**SI Fig. 1g**) contains the emission filter (**SI Fig. 1h**) and dichroic mirror (**SI Fig. 1i**). The fluorescence LED (**SI Fig. 1j**) is soldered to a PCB with a male 2-pin JST connector and 10-Ω resistor; this PCB assembly slides into a slot in the CFM clamshell holder aligned to the excitation filter (**SI Fig. 1k**) in an adjacent slot, pointing towards the fluorescence cube adapter (**SI Fig. 1l**) that holds the fluorescence cube. The adapter screws into the tube above it and the tube below it. The tube below it (**SI Fig. 1m**) holds an RMS-SM1 adapter (**SI Fig. 1n**) that holds the objective (**SI Fig. 1o**). The sample cell holder (**SI Fig. 1p and 1q**) screws into this objective tube until the sample inside the holder is in focus. The sample is backlit by the brightfield LED (**SI Fig. 1r**) soldered to a PCB with a male 2-pin JST connector and 10-kΩ resistor.

SI Note 3: Cutting the annular tape rings

A 3" wide strip of 3M double sided masking tape (uline.com) was adhered to an 8.5” × 11” sheet of heavy weight cardstock printer paper. The 3M tape cover paper was removed and saved. Then a three-inch-wide strip of double-sided Kapton polyimide tape (kaptontape.com) was placed, cover paper down, onto the 3M tape adhering the 3M cover paper on top of the Kapton tape. The tape assembly was then loaded into a craft cutter (Silhouette Cameo 2) with the blade at the deepest cut position (#10) and the pressure and speed set at the factory settings. The annular circle dimensions (I.D. = 7 mm, O.D. = 15 mm) were drawn in the Silhouette software in a repeating pattern and sent to the Silhouette cutter for cutting. After the cutting is finished, the tape assembly was removed from the cutter.

SI Note 4: Particle Tracking

While a variety of methods for particle tracking are available (e.g. centroid, Gaussian), we chose a radial symmetry method for its accuracy, speed, and MATLAB graphical user interface.[1] This method was developed as a faster and more flexible alternative to the Gaussian centroid method.

It is two orders of magnitude faster than Gaussian methods (important for large data sets) because it does not need to measure the amplitude and width of the intensity distribution. It is more flexible because it can be applied to any radially symmetric particle, including concentric rings. It is also better than the Gaussian methods at differentiating two particles close enough together that their intensity profiles overlap. The method works by drawing a line through every pixel of the object, with each line being parallel to the intensity gradient at that pixel. For a radially symmetrical particle, each line will intersect the center of the particle. Even for radially asymmetric particles, this method is as accurate as Gaussian methods.

SI Note 5: Derivation of microsphere settling velocity

For a spherical microbead settling through a Newtonian liquid, the drag force acting on the particle is $F_d = 6\pi\eta a v$, where F_d is the frictional force, η is the dynamic viscosity of the fluid, a is the radius of the particle, and v is the settling velocity of the particle. The gravitational force acting on this particle is $F_\mathrm{g} = (\rho_\mathrm{c} - \rho_\mathrm{f}) g \frac{4}{3}\pi a^3$, where ρ_c is the density of the particle, ρ_f is the density of the fluid, and g is the acceleration due to gravity. Balancing the two force equations and solving for the velocity v, provides terminal velocity v_t of the particle. We assume v_t is reached in a very short time, much less than the settling time.

SI Note 6: Manual Image Counting Analysis of Microsphere Detachments

MATLAB image analysis was performed manually frame-by-frame (for every one out of 100 frames) to count the number of particles that detach in each frame. The number of particles detached from each frame to the next was recorded in a spreadsheet. The frame-by-frame particle counts were added together across three runs at each experimental condition, synced with the speed data to determine the effective gravity acting on the particles in each frame, and then binned as a function of effective gravitational force in MATLAB The “histogram” command was used to generate the normalized probability distribution according to predefined bin limits, and the “counts” command was used to retrieve the bin *y*-axis values so they could be plotted and fitted in a plotting software (**Fig. 5F**).

SI Note 7: Assumptions for the Gregory model of predicting detachment force

The theoretical van der Waals force was calculated using $F_\mathrm{vdw} = Aa/(6h(1+14h/\lambda))$ where A is the Hamaker constant, a is the particle radius, h is the separation distance, and λ is the characteristic wavelength of retardation, typically assumed to be 100 nm. This model of F_vdw is similar to the simpler model derived by Hamaker[2] and by Israelachvili,[3] but is more accurate for very small separation distances and up to about 0.2× the particle radius.[4, 5]

The Van der Waals force F_{vdw} at a given separation distance h is largely dependent on the Hamaker constant A_{132}, which is dependent on the refractive indices (n_i) and relative permittivities (ε_i) of the two objects (materials 1 and 2) and the medium separating them (material 3) as $A_{132} = 3kT((\varepsilon_1 - \varepsilon_3)/(\varepsilon_1 + \varepsilon_3))((\varepsilon_2 - \varepsilon_3)/(\varepsilon_2 + \varepsilon_3))/4 + 3h\nu((n_1^2 - n_3^2)(n_2^2 - n_3^2)/\sqrt{}((n_1^2 + n_3^2)(n_2^2 + n_3^2)(\sqrt{}(n_1^2 + n_3^2) + \sqrt{}(n_2^2 + n_3^2))/8\sqrt{2}$. Glass (material 1) and aqueous electrolyte (material 3) are well characterized,[3] as is polystyrene, but polystyrene/iron oxide is not well characterized. These microspheres are a homogeneous mixture of iron oxide nanoparticles in a polystyrene polymer matrix, with at least 20% composition iron oxide by mass. Thus, to determine the Hamaker constant of the microsphere composite material, we used the mass average of the refractive indices and relative permittivities of polystyrene and iron oxide ($n_{ps} = 1.557$, $n_{iro} = 1.97$, $\varepsilon_{ps} = 2.55$, $\varepsilon_{iro} = 14.2$), assuming an iron oxide mass fraction of 0.2, and arrived at a Hamaker constant for our system of $A_{132} = 13.2 \times 10^{-21}$ J. The Hamaker constant is, however, screened in aqueous electrolytes,[6] so we multiplied the Hamaker constant by a factor of 2/3 to arrive at a value of $A_{132} = 8.77 \times 10^{-21}$ J.

The theoretical electrostatic force is calculated by $F_{el} = \kappa 64\pi\varepsilon a(kT/ze)^2\gamma_1\gamma_2\exp[-\kappa h]$ where κ is the inverse Debye length $\kappa = \sum\sqrt{}(n_i e^2 z_i^2/\varepsilon kT)$, n_i is the number density of the i^{th} ion species, ε is the permittivity of the solution, a is the particle radius, k is the Boltzmann constant, T is the absolute temperature, z_i is the valence of the i^{th} ion species, e is the charge of an electron, and $\gamma_1 = \tanh(ze\psi/4kT)$ where ψ is the surface potential and h is the separation distance. This model was also developed by Gregory[7] and has been used for approximating practical conditions where a middle ground between the constant charge and constant potential boundary conditions used in deriving these conditions is considered more appropriate.[4, 8, 9]

The electrostatic force F_{el} is largely dependent on the glass surface potential ψ_g, the polystyrene microsphere surface potential ψ_{cs}, and the inverse Debye length κ^{-1}. The Debye length is well defined based on the aqueous electrolyte concentration, but the surface potentials ψ_{cs} and ψ_g are quite uncertain. Polystyrene spheres are manufactured using emulsion polymerization and are stabilized by the negatively charged sulfate surface groups that result from the production process. Depending on the exact procedure used during production, polystyrene spheres can have a range[10] of surface charge densities from 0.002 - 0.025 C/m^2 (based on reference [14] and on reported data from Thermo Fisher carboxyl latex microspheres such as p/n C37281), and the zeta potential ζ is usually observed[11-15] to be 40 – 1000 mV in pure or low electrolyte water. The zeta potential is also reported to decrease with increasing electrolyte concentration, down to around 20 – 40 mV, but models also suggest that low ζ at high ionic strength solutions may represent significantly higher surface potentials than are observed.[16] In general, across most ionic strengths, the true surface potential is assumed to be at least somewhat higher than ζ. The same issues apply for glass ψ_g. Our treatment process includes sonication in NaOH, which has been shown to make the glass highly negatively charged,[17] up to 0.76 C/m^2 at 1.0 M NaOH, which using the Gouy-Chapman model[15, 18] results in a surface potential of 350 mV. Glass has also been well characterized in aqueous electrolyte,[19-22] but, to our knowledge, no one has reported how long NaOH treatment effects last and if they persist after drying and immersing in aqueous electrolyte. Therefore, we take ranges of values from the literature and assume the glass is relatively highly charged at ψ_g = 150 – 300 mV and the polystyrene microspheres are low to moderately charged at ψ_{cs} = 30 – 100 mV, keeping in mind that the true values may deviate even further than this range. The predicted detachment forces for these ranges are shown as the upper and lower gray dashed lines in **Figure 5E**. Our experimentally measured values at high ionic strength (Fig. 5E, blue circles) are lower than the predicted values (Fig. 5E, gray dashed lines). This is likely due to the aforementioned surface charge uncertainty[11-15, 23-25] as well as surface roughness[22, 26-31] and spatial heterogeneities of the glass substrate surface potential.[32-35]

SI Figures:

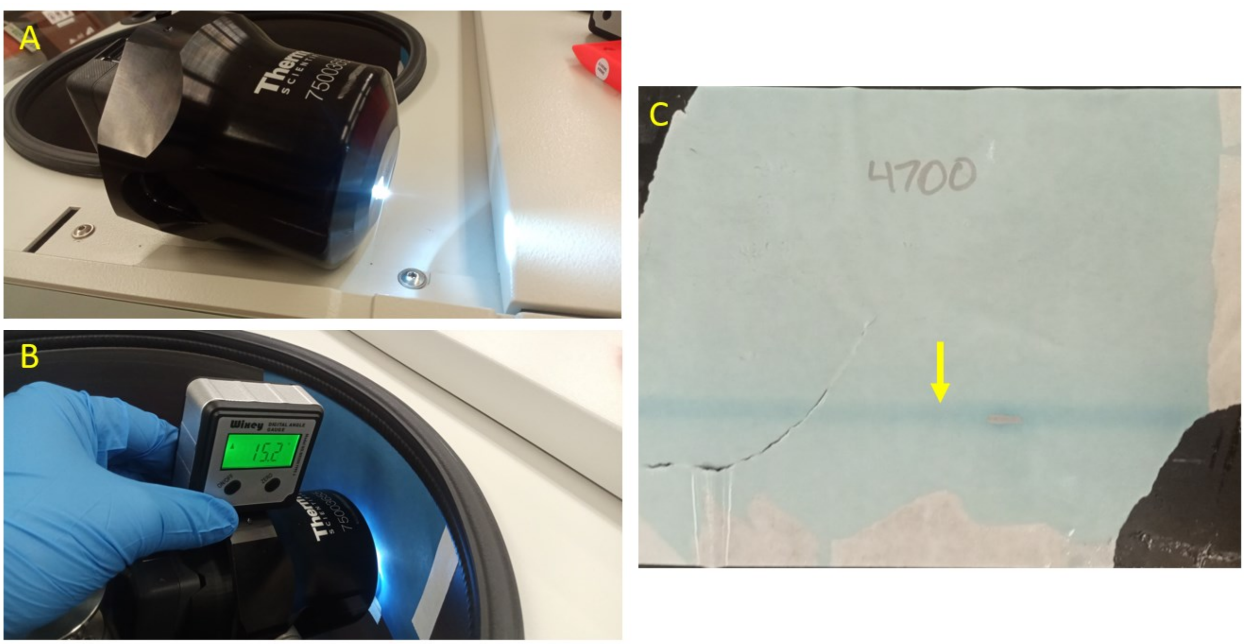

SI Figure 1: *Measuring the swinging bucket angle at different rotational velocities*. The bucket angle at different rotational velocities was measured using light sensitive cyanotype paper. (**A**) A hole was drilled in the bottom of a centrifuge bucket and an LED was installed to point downward out of the bucket. (**B**) A sheet of cyanotype paper was taped to the inside of the centrifuge. After the centrifuge run was complete, and a digital protractor was used to measure the angle required to create (**C**) the light-developed line in the cyanotype paper.

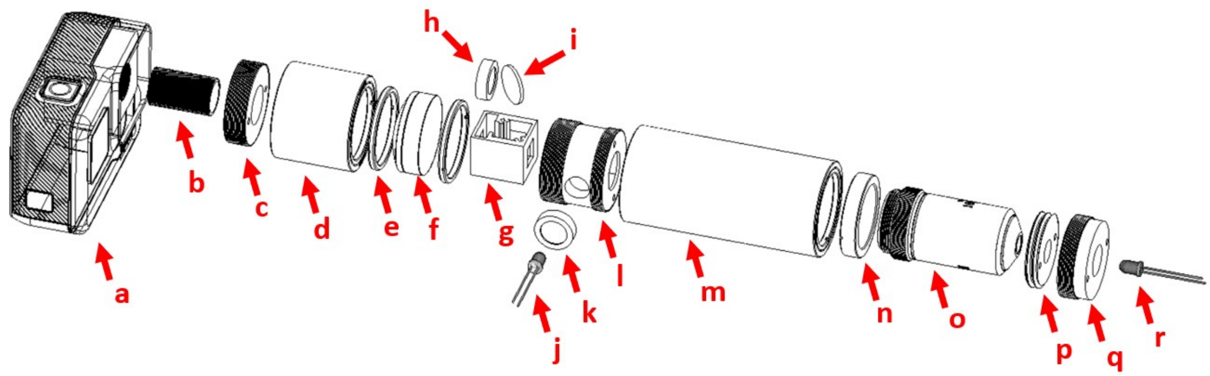

FIG. REF.	VENDOR	PART NUMBER	DESCRIPTION	PRICE
a	Gopro	n/a	Hero 5 Black action camera	$180.00
b*	n/a	n/a	M12 1-inch adapter, fabricated	$50.00
c	Thorlabs	SM1TM12	SM1 to M12 x 0.5 Lens Cell Adapter	$22.00
d	Thorlabs	SM1M10	SM1 Lens Tube Without External Threads, 1" Long	$13.87
e	Thorlabs	n/a	Retaining ring (included with lens tube)	$0.00
f	Thorlabs	AC254-030-A	f=30.0 mm, 1" Dia. Achromatic Doublet, ARC: 400-700 nm	$82.62
g	n/na	n/a	Fluorescence Cube, 3D Printed	$0.00
h	Edmund Optics	67016	Emission Filter 520NM x 36 NM BP 93T 12.5D	$185.00
i	Edmund Optics	67055	Filter Dichroic 495NM 12.5D	$140.00
j**	Adafruit		Diffused white LED	$5.00
k	Edmund Optics	67013	Excitation Filter 472NM x 30 NM BP 93T 12.5D	$185.00
l	n/a	n/a	Fluorescence Cube Adapter, 3D printed	$0.00
m	Thorlabs	SM1M25	SM1 Lens Tube Without External Threads, 2.5" Long	$17.44
n	Thorlabs	SM1A3	Adapter with External SM1 Threads and Internal RMS Threads	$17.44
o	Boli Optics	BM13063431	Objective 20X 5.1mm WD Infinity Plan Achromat	$89.98
p	n/a	n/a	Sample cell holder top, 3D printed	$0.00
q	n/a	n/a	Sample cell holder bottom, 3D printed	$0.00
r***	Mouser Electronics	C503B-BAN-CX0B0461	Standard LEDs - Through Hole Blue Round - 5mm dia - T-1 3.4 - 470 nm	$5.00
n/a	Amazon	EL-CK-004	Elegoo resistor kit 0 Ω - 1 MΩ (10 kΩ resistor)	$13.86
n/a	Digi-key	B2B-PH-K-S(LF)(SN)	JST 2-pin male connector	$0.17
n/a	Amazon	EL-CK-004	Elegoo resistor kit 0 Ω - 1 MΩ (10 Ω resistor)	$0.00
n/a	Amazon		Neutral Density Filter, ND1.2, 4 F-Stop, Rosco E Colour 299	$9.00
				$1,016.38

SI Figure 2: *Exploded F-CFM diagram and parts information*.
*Fabricated using M12 × 0.5 metric right-hand thread die, manual die holder, manual pipe cutter, and 12-mm OD aluminum tubing, all purchased from Amazon.
**Soldered to PCB with 10-kΩ resistor and through-hole male JST PH 2-pin connector (Digi-Key p/n 455-1704-ND). PCB is designed in Eagle CAD and ordered from OshPark.

*** Soldered to PCB with 10-Ω resistor and through-hole male JST PH 2-pin connector (Digi-Key p/n 455-1704-ND). PCB is designed in Eagle CAD and ordered from OshPark. Powered by LiPo battery (Sparkfun p/n PRT-13813).

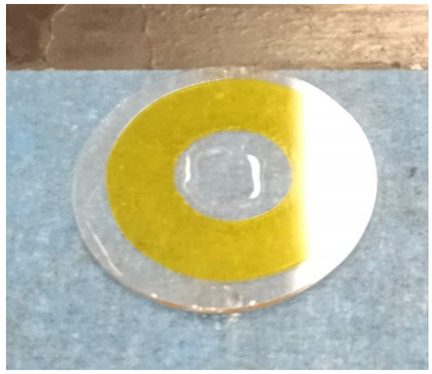

SI Figure 3: *Assembled sample cell.* The adhesive bead "bubble barrier" is visible as the square shape inside the annular golden colored Kapton tape ring sandwiched between two glass cover slips.

SI Figure 4: *Images of the F-CFM unit and centrifuge.* (**A**) The F-CFM module can be seen in the centrifuge buckets at the 6:00 o'clock and 12:00 o'clock positions. (**B**, **C**) Images of the polycarbonate enclosure.

SI Tables:

SI Table 1: Fitting form and parameters for Figure 2B (main text).

Fit equation: $AR_{hole} = a + bR + cR^2 + dR^3 + eR^4 + fR^5$

Fit parameter	Value
a	1.06
b	0.000135
c	-2.54e-6
d	2.60e-8,
e	4.80e-11
f	2.49e-14
R	0.876

SI Table 2: Log-normal fit parameters for detachment force probability distributions in Figure 5F (main text). Fit equation: $P_d(F_d) = d(\exp[-\ln(F_d)/c]^2)/(2b^2))/(F_d b\sqrt{\pi})$.

	NaCl concentration (M)							
Fit Parameter	0.1	0.1 error	0.5	0.5 error	1.25	1.25 error	2.5	2.5 error
b	1.350	0.06666	1.113	0.05990	0.6925	0.04231	0.6366	0.03254
c	0.5931	0.04765	1.143	0.1133	1.154	0.05916	1.824	0.07036
d	0.2156	0.01076	0.2260	0.01592	0.1919	0.01170	0.1960	0.009828
R	0.9825		0.9306		0.9286		0.9427	

SI Table 3: Power fit parameters for predicted detachment force curves in Figure 5E (main text).

Fit equation: $F_{d,mode}(I) = p(I)^q$

Fit Parameter	Lower Curve	Upper Curve

p	0.6254	1.029
q	1.448	1.521
R	0.9999	0.9998

References Cited

1. R. Parthasarathy, *Nature Methods*, 2012, **9**, 724-726.
2. H. C. Hamaker, *Physica*, 1937, **4**, 1058-1072.
3. J. N. Israelachvilli, 1985, 1-674.
4. S. Assemi, J. Nalaskowski and W. P. Johnson, *Colloids and Surfaces A: Physicochemical and Engineering Aspects*, 2006, **286**, 70-77.
5. J. Gregory, *Journal of Colloid and Interface Science*, 1981, **83**, 138-145.
6. M. A. Bevan and D. C. Prieve, *Langmuir*, 1999, **15**, 7925-7936.
7. J. Gregory, *Journal of Colloid and Interface Science*, 1974, **51**, 44-51.
8. M. Elimelech, J. Gregory, X. Jia and R. Williams, *Butterworth-Heinemann Ltd*, 1995.
9. C. Chen, K. S. Liu and J. Y. Shang, *Journal of Soils and Sediments*, 2018, **18**, 1066-1075.
10. S. L. Tsaur and R. M. Fitch, *Journal of Colloid and Interface Science*, 1987, **115**, 450-462.
11. K. M. Ohsawa, M.; and Ohshima, H., *Colloid & Polymer Science*, 1986, **264**, 1005-1009.
12. R. Folkersma, A. J. G. van Diemen and H. N. Stein, *Langmuir*, 1998, **14**, 5973-5976.
13. Z. Adamczyk, A. Bratek-Skicki, P. Dabrowska and M. Nattich-Rak, *Langmuir*, 2012, **28**, 474-485.
14. W. M. Brouwer and R. L. J. Zsom, *Colloids and Surfaces*, 1987, **24**, 195-208.
15. E. C. Y. Yan, Y. Liu and K. B. Eisenthal, *Journal of Physical Chemistry B*, 1998, **102**, 6331-6336.
16. J. Lyklema and J. T. Overbeek, *Journal of Colloid Science*, 1961, **16**, 501-&.
17. J. M. Rimsza, R. E. Jones and L. J. Criscenti, *Journal of Colloid and Interface Science*, 2018, **516**, 128-137.
18. K. S. Elassy, M. A. Rahman, N. S. Yama, W. A. Shiroma and A. T. Ohta, *IEEE Access*, 2019, **7**, 150150-150156.
19. Y. G. Gu and D. Q. Li, *Journal of Colloid and Interface Science*, 2000, **226**, 328-339.
20. B. J. Kirby and E. F. Hasselbrink, *Electrophoresis*, 2004, **25**, 187-202.
21. D. Erickson, D. Q. Li and C. Werner, *Journal of Colloid and Interface Science*, 2000, **232**, 186-197.
22. G. Trefalt, T. Palberg and M. Borkovec, *Current Opinion in Colloid & Interface Science*, 2017, **27**, 9-17.
23. A. Garg, C. A. Cartier, K. J. M. Bishop and D. Velegol, *Langmuir*, 2016, **32**, 11837-11844.
24. O. El-Gholabzouri, M. A. Cabrerizo and R. Hidalgo-Alvarez, *Journal of Colloid and Interface Science*, 1999, **214**, 243-250.
25. Y. Tabata and Y. Ikada, *Biomaterials*, 1988, **9**, 356-362.
26. R. M. Pashley, P. M. McGuiggan, B. W. Ninham and D. F. Evans, *Science*, 1985, **229**, 1088-1089.
27. Y. I. Rabinovich, J. J. Adler, A. Ata, R. K. Singh and B. M. Moudgil, *Journal of Colloid and Interface Science*, 2000, **232**, 10-16.
28. Y. I. Rabinovich, J. J. Adler, A. Ata, R. K. Singh and B. M. Moudgil, *Journal of Colloid and Interface Science*, 2000, **232**, 17-24.
29. K. Cooper, A. Gupta and S. Beaudoin, *Journal of Colloid and Interface Science*, 2000, **228**, 213-219.
30. K. Cooper, N. Ohler, A. Gupta and S. Beaudoin, *Journal of Colloid and Interface Science*, 2000, **222**, 63-74.
31. H. J. Butt, B. Cappella and M. Kappl, *Surface Science Reports*, 2005, **59**, 1-152.
32. Y. Luthi, J. Ricka and M. Borkovec, *Journal of Colloid and Interface Science*, 1998, **206**, 314-321.

33. A. M. Schrader, J. I. Monroe, R. Sheil, H. A. Dobbs, T. J. Keller, Y. X. Li, S. Jain, M. S. Shell, J. N. Israelachvili and S. G. Han, *PNAS*, 2018, **115**, 2890-2895.
34. J. J. Cras, C. A. Rowe-Taitt, D. A. Nivens and F. S. Ligler, *Biosensors & Bioelectronics*, 1999, **14**, 683-688.
35. P. Warszynski and Z. Adamczyk, *Journal of Colloid and Interface Science*, 1996, **1878**, 283-295.